

An error indicator for finite difference methods using spectral techniques with application to aerofoil simulation

Christian T. Jacobs^{a,*}, Markus Zauner^a, Nicola De Tullio^a, Satya P. Jammy^a, David J. Lusher^a, Neil D. Sandham^a

^a*Aerodynamics and Flight Mechanics Group, Faculty of Engineering and the Environment, University of Southampton, University Road, Southampton, SO17 1BJ, United Kingdom*

Abstract

This work introduces a new error indicator which can be used to determine areas of insufficient numerical resolution in unfiltered finite difference simulations. The background behind the methodology is that smaller scales (i.e. the flow features with higher wave numbers) are physically characterised by a smaller energy content in comparison with larger scales. This energy should decrease with increasing wavenumber at a minimum rate; if this rate is not attained it likely means that the smaller scales are not being properly resolved on the computational grid of solution points. An approach using spectral techniques is used to formulate two varieties of the error indicator – one integer-valued and one floating point-valued. These values are computed at a finite number of ‘blocks’ which span the domain. The indicator is implemented within the OpenSBLI finite difference-based modelling framework, and evaluated in the context of a three-dimensional Taylor-Green vortex problem and flow past a V2C laminar flow aerofoil.

Keywords: Error indicators, Finite difference methods

*Corresponding author.
E-mail address: C.T.Jacobs@soton.ac.uk

1. Introduction

Computational grids are at the core of many numerical models. They comprise a set of points upon which the governing equations are solved. One of the crucial constraints of grid generation is that small-scale structures must be sufficiently well resolved by the grid, since any errors (introduced through numerical dispersion and dissipation, as well as nonlinear effects such as aliasing) can cause the simulation to become inaccurate and unstable [1]. Adopting a uniformly-fine grid to ensure this constraint is satisfied often results in a large number of superfluous grid points, which is detrimental to the model's computational efficiency. At the same time, it is often not possible to know *a priori* exactly where high resolution needs to be placed in the domain, particularly when dealing with transient and turbulent dynamics frequently encountered in real-world applications. The formulation of *a posteriori* error estimators and indicators, and their coupling with adaptive grid refinement methods, has therefore attracted a considerable amount of attention over the last few decades (e.g. [2]).

The current work is focussed on finite difference solutions of the compressible Navier-Stokes equations in the absence of explicit filtering or artificial dissipation. Such an approach is commonly used for DNS [3]. A feature of under-resolved regions of flow is the appearance of grid-to-grid point oscillations, usually first apparent in derivative quantities such as vorticity or dilatation rate. Typically the appearance of such numerical errors/oscillations is used to decide when and where grid refinement is required. This work aims to quantify and calibrate these features of under-resolution such that the grid refinement process can ultimately be automated.

A new error indicator, based on spectral techniques using small-domain Fourier transforms, is presented herein. It does not attempt to quantify the solution error, but instead estimates the severity of any under-resolution that occurs in the solution field. The indicator is implemented in the OpenSBLI finite difference modelling framework [4]. Section 2 describes the error indicator in further detail. It is then evaluated in Section 3 by considering three-dimensional simulations of the Taylor-Green vortex problem [5] and flow past a V2C laminar aerofoil (see e.g. [6]). Some conclusions are drawn in Section 5.

2. Error Indicator

The error indicator considers a finite number of small cubes which together span the whole 3D domain. For each N_e^3 block, and for each line of N_e points within it, various Fourier amplitudes of a user-specified solution field are computed. These amplitudes are subsequently averaged over N_e^2 lines to determine the anisotropic error ‘severity’ values.

The first step to computing the error indicator is to apply a Hamming window to the solution field y , in order to ensure its smoothness and periodicity for Fourier analysis. Thus for each line of N_e solution points in each direction:

$$y_j = y_j \frac{\left(0.54 - 0.46 \cos\left(\frac{2\pi j}{N_e}\right)\right)}{0.54}, \quad (1)$$

where y_j is the j -th component of the solution field y in the line of solution points under consideration.

The Fourier amplitudes (proportional to the square root of the spectral energy) for selected modes/wavenumbers $N_e/2$, $N_e/4$ and $N_e/8$ of the solution field are then computed, for each N_e^3 block. In order to avoid doing a computationally intensive Fourier transform each time, the amplitudes are reconstructed by using simple summations, S :

$$S_2 = \sum_{j=0}^{N_e-1} (-1)^j y_j, \quad (2)$$

$$S_4 = \sum_{j=0}^{N_e-1} (-i)^j y_j, \quad (3)$$

$$S_8 = \sum_{j=0}^{N_e-1} \exp\left(-\frac{\pi}{4}i\right)^j y_j, \quad (4)$$

where $i = \sqrt{-1}$. These values were checked for correctness against a fast Fourier transform.

With an increasing mode/wavenumber k , we desire the spectral energy $E(k)$ (and therefore the mode amplitude $Y(k)$) to decrease at a minimum rate, such that the smallest scales have the lowest energy content. An increase in $E(k)$, for example due to aliasing errors arising from non-linear terms,

is likely to mean that we are not resolving the small scales well enough. Determining where this increase occurs in the domain facilitates the dynamic focussing of resolution in that area. To this end, the error indicator presented here is based on detecting whether the spectrum decay rate is worse than some prescribed value.

Two versions of the error indicator, denoted I_i and I_f , were developed; I_i is integer-valued while the other, I_f , is floating-point-valued. These are defined as

$$I_i = \begin{cases} 1, & \text{if } A_2 > A_4 + \varepsilon \\ 0, & \text{otherwise} \end{cases} + \begin{cases} 1, & \text{if } A_4 > A_8 + \varepsilon \\ 0, & \text{otherwise} \end{cases} + \begin{cases} 1, & \text{if } A_2 > A_8 + \varepsilon \\ 0, & \text{otherwise} \end{cases} \quad (5)$$

$$I_f = \log \left(1 + \lfloor \frac{A_2}{A_4 + \varepsilon} \rfloor + \lfloor \frac{A_4}{A_8 + \varepsilon} \rfloor + \lfloor \frac{A_2}{A_8 + \varepsilon} \rfloor \right), \quad (6)$$

where $\lfloor \dots \rfloor$ is a ‘floor’ operation, and the values A_2 , A_4 and A_8 are defined as

$$A_2 = 2^{-2r} \left| \frac{S_2}{N_e} \right|, \quad (7)$$

$$A_4 = 2^{-r} \left| \frac{2S_4}{N_e} \right|, \quad (8)$$

$$A_8 = \left| \frac{2S_8}{N_e} \right|, \quad (9)$$

which (in the case of a 3D domain) are computed in each direction along N_e^2 lines. The small value ε (set to 10^{-2} in Section 3 and 3×10^{-2} in Section 4) is used to avoid division-by-zero problems in uniform flow conditions. Note that either the maximum or mean of these A values can be taken, thereby generating slightly different variants of I_i and I_f . It was found *a posteriori* that considering the maximum values in each block seems to make the indicators I_i and I_f more sensitive compared to taking the mean values (an operation that likely smears out any under-resolution effects). Therefore, only the maximum values are considered in this paper.

The quantity I_i is an integer in the set $\{0, 1, 2, 3\}$, where a value of 3 indicates the worst possible error according to the error indicator, and 0 indicates that no error is present. In contrast, the quantity I_f is a real value

80 bounded below by zero (which indicates that little or no solution error is
 81 present). Deciding what constitutes an ‘unacceptably high’ value depends
 82 on the specific problem at hand. One of the caveats of the approach is
 83 the need to estimate the minimal acceptable slope r of the mode amplitude
 84 line. For example, this could be taken to decrease with a slope of $r=-5/6$
 85 for turbulent dynamics (following Kolomogorov’s $k^{-5/3}$ law for the inertial
 86 subrange of the spectral energy spectrum), but in practise r will be higher or
 87 lower locally; throughout this paper we consider a slope value of $r = -0.5$. If
 88 shocks are present, then a slope of -1 (following the k^{-2} law for discontinuities
 89 [7]) may be more appropriate. Note also that the slope r may also depend
 90 on the behaviour of the solution field/quantity being considered. The typical
 91 values mentioned so far correspond to the decay of energy, but it was found
 92 *a posteriori* that these values also worked well for vorticity which followed
 93 a similar decay pattern. Nevertheless, it is important to remember that the
 94 desired slope may vary depending on the chosen quantity and problem.

95 **3. Test Case: Compressible Taylor-Green Vortex**

96 A three-dimensional compressible Taylor-Vortex problem (see e.g. [5]) in
 97 a periodic cube domain of length 2π was used to evaluate the effectiveness of
 98 the error indicator. This considered a fourth-order finite difference solution
 99 without additional filtering on computational grids of size $N = 32^3, 64^3, 128^3$
 100 and 256^3 . The robustness of the error indicator was improved by considering
 101 overlapping blocks, with the grid point count per block remaining the same.
 102 The number of blocks in each direction was set to 7 such that each block
 103 contained $(N/4)^3$ solution points. This provided an error severity value every
 104 $N_e/2$ points in all directions. The $N=32^3$ case adopted a non-dimensional
 105 time-step Δt of 6.77×10^{-3} [5]. As the grid was refined, the time-step size
 106 was halved. The simulation was run until non-dimensional time $T = 20$. All
 107 simulations considered here were performed on a single NVIDIA Tesla K40c
 108 GPU. Further details of the simulation setup can be found in [4], where it
 109 is shown that a grid of at least 256^3 points should be employed to give close
 110 agreement with reference data [8].

111 The indicator computed the severity of under-resolution in the z -component
 112 of the vorticity field, denoted $(\nabla \times \mathbf{u})_z$, every 100 iterations. The 32^3 grid
 113 greatly under-resolved the turbulent dynamics and, particularly around the
 114 point of peak enstrophy, displayed grid-to-grid point oscillations as a result.
 115 As the grid was refined the overall severity of the solution error was reduced.

116 This is illustrated in Table 1 which shows a reduction in the maximum values
 117 of I_i and I_f across both space and time. The small increase of I_f in the 64^3
 118 case was caused by an intermittently-high severity value at early times ($t =$
 119 5–6); an even larger value of ε would be required to suppress this anomalous
 120 behaviour.

121 A clearer visualisation is provided in Figure 1 which displays a general
 122 reduction in the number of high severity values of I_i throughout time. Larger
 123 errors were particularly noticeable around non-dimensional time $t = 9$ – 10 at
 124 the point of peak enstrophy where the flow becomes fully turbulent, suggest-
 125 ing that further grid refinement is necessary to properly resolve the turbulent
 126 fluctuations. Due to the symmetry of the problem and the domain-wide tur-
 127 bulence, refinement is often shown to be necessary in large portions or even
 128 all of the domain; the real benefits of error indicators and their coupling with
 129 grid refinement techniques will become apparent when such an approach is
 130 applied to more realistic flow problems where turbulent dynamics that re-
 131 quire higher resolution may only be present in a small section of the domain.

Grid size	$\max(I_i)$	$\max(I_f)$
32^3	3	1.945910
64^3	3	2.197225
128^3	2	1.386294
256^3	1	0.693147

Table 1: Grid sizes considered in the Taylor-Green vortex simulation and the maximum severity value of the error indicators over all I/O dumps.

132 4. Application: V2C laminar flow aerofoil

133 The error indicator was applied to a three-dimensional direct numerical
 134 simulation of transonic, compressible flow past a V2C laminar flow aerofoil (a
 135 profile designed by Dassault Aviation [6]) at an incidence $\alpha = 4^\circ$, Reynolds
 136 number based on the aerofoil chord $Re_c = 5 \times 10^5$ and Mach number $M = 0.7$.

137 The computational domain is illustrated in Figure 2 and partitioned
 138 into three blocks, with interface boundary conditions between neighbouring
 139 blocks. The domain dimensions are $R = 7.5c$ and $W = 6c$ with a spanwise
 140 extension of $L_z = 0.05c$. Blocks 1 and 3 are associated with Cartesian grids
 141 stretched in the x and y directions such that more resolution is present near

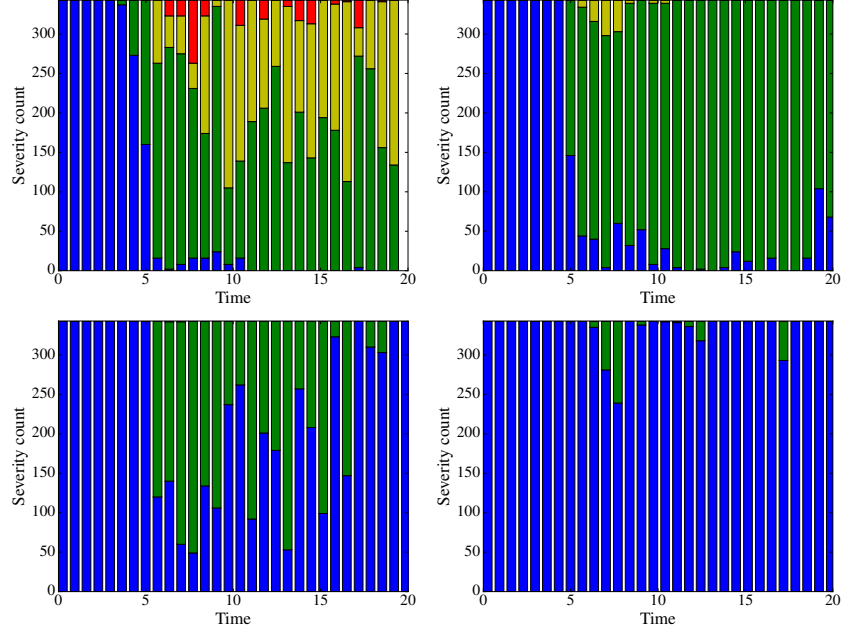


Figure 1: The counts of all the error indicator values across the entire domain for 32^3 , 64^3 , 128^3 and 256^3 grids (top-left to bottom-right), using overlapping blocks. Blue, green, yellow and red indicate I_i error severity values of 0, 1, 2 and 3, respectively.

the trailing edge of the aerofoil and in the wake. Block 2 contains the aerofoil itself and is associated with a C-grid, with resolution being focused near the leading and trailing edges and near the wall.

The V2C aerofoil profile has a blunt trailing edge and therefore two singular points at the corners. The grid points resolving the trailing edge surface are contained in blocks 1 and 3. The grid lines containing the corners of the blunt trailing edge are designed as a continuous extension of the aerofoil geometry. A corner treatment is applied according to the trailing edge treatment used by Jones [9]. In order to increase the numerical stability of supersonic flows, a total variation diminishing (TVD) scheme is applied to capture shock waves. Characteristic conditions were enforced at all the domain boundaries in order to minimise wave reflections. In particular, a zonal characteristic boundary condition [10] is applied over a distance $L_{zonal} \approx 0.45c$ near the outflow boundary of blocks 1 and 3, using 51 grid points. An integral characteristic condition [11] is applied at the other boundaries where, in

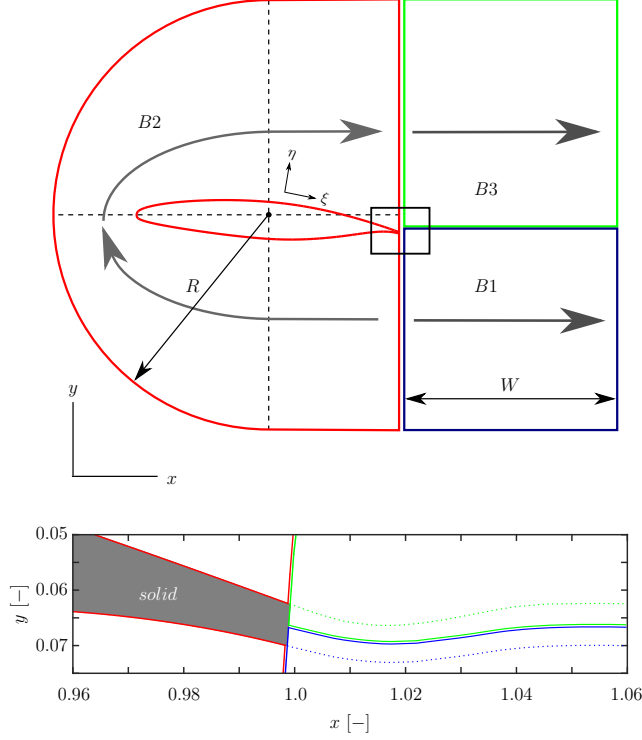


Figure 2: Sketch of the computational domain. Block 2 (denoted B2) contains the V2C aerofoil, while blocks 1 and 3 (B1 and B3) are resolving the wake line.

157 addition, the free-stream solution is imposed at each time-step. The aerofoil
 158 is modelled using a no-slip, isothermal boundary condition, with the wall
 159 temperature equal to the free-stream temperature.

160 A summary of the two computational grids employed is given in Table
 161 2; the first is relatively coarse, and the second is a refined version with
 162 more resolution placed near laminar-turbulent transition regions and along
 163 the wake path. The two simulations were carried out on the UK National
 164 Supercomputing Service (ARCHER). Fourth-order central differences with a
 165 Carpenter scheme near boundaries [12], and a third-order low-storage Runge-
 166 Kutta timestepping scheme (with a time step of $\Delta t = 2 \times 10^{-5}$), were used.

167 The error indicator implemented in the OpenSBLI code was once again
 168 applied to the z -component of the vorticity field. However, the simulation
 169 itself was performed using the legacy Fortran-based SBLI code [13] (because
 170 characteristic boundary conditions were not available in OpenSBLI at the

R/c	W/c	L _z /c	N _{ξ,2}	N _{η,2}	N _{ξ,1/3}	N _{η,1/3}	N _z	N _{total}
7.5	6.0	0.05	2095	999	999	1023	50	2.07×10^8
7.5	6.0	0.05	3045	999	1999	1023	150	1.07×10^9

Table 2: Numerical grid details for the grid before (first row) and after refinement (second row). Note that N_{ξ,2} and N_{η,2} are the number of grid points of block 2 around the aerofoil in the ξ and η direction, respectively, whereas N_{ξ,1/3} and N_{η,1/3} denote the number of grid points in block 1 and block 3 to resolve the wake (see Figure 2). N_z is the spanwise resolution and N_{total} denotes the total number of grid points.

171 time of writing) and the solution fields were read into OpenSBLI from a
172 binary file. Each error indicator block comprised 16^3 grid points.

173 Error severity values of I_i near the aerofoil when the flow was fully de-
174 veloped are shown in Figure 3. The uniform flow away from the aerofoil
175 is relatively well-resolved by both grids as suggested by I_i values of 0 or
176 1. The flow dynamics in the vicinity of the aerofoil are characterised by a
177 separation of the laminar boundary layer on both sides of the aerofoil, fol-
178 lowed by a laminar-turbulent transition of the separated flow and turbulent
179 flow reattachment just downstream of the mid-chord position. The process
180 of turbulent flow separation/reattachment gives rise to a highly unsteady
181 wake downstream of the aerofoil. In the case of the coarse grid, a signifi-
182 cant number of $I_i = 2$ and $I_i = 3$ values suggested that these latter areas of
183 the domain exhibiting turbulent dynamics were heavily under-resolved. The
184 grid was therefore manually refined around the trailing edge of the aerofoil
185 and in the wake region, which resulted in a reduction in error severity (the
186 presence of mainly $I_i = 0$ and $I_i = 1$ values) and the adequate resolution of
187 the turbulent structures. This demonstrates how the error indicator can be
188 used to help target refinement strategies.

189 The dominant flow structures in the transitional separation region on ei-
190 ther side of the aerofoil are represented by Kelvin-Helmholtz rollers. The
191 interaction between these structures and the trailing edge leads to the scat-
192 tering of acoustic waves that sustain the laminar-turbulent transition. The
193 global modes caused by these acoustic waves are likely to be the cause of the
194 occasional $I_i = 1$ values away from the aerofoil where the flow appears to be
195 uniform. The cluster of $I_i = 2$ and $I_i = 3$ values at the leading edge is due
196 to the thin boundary layer and has been addressed with a combination of
197 further grid refinement and localised filtering.

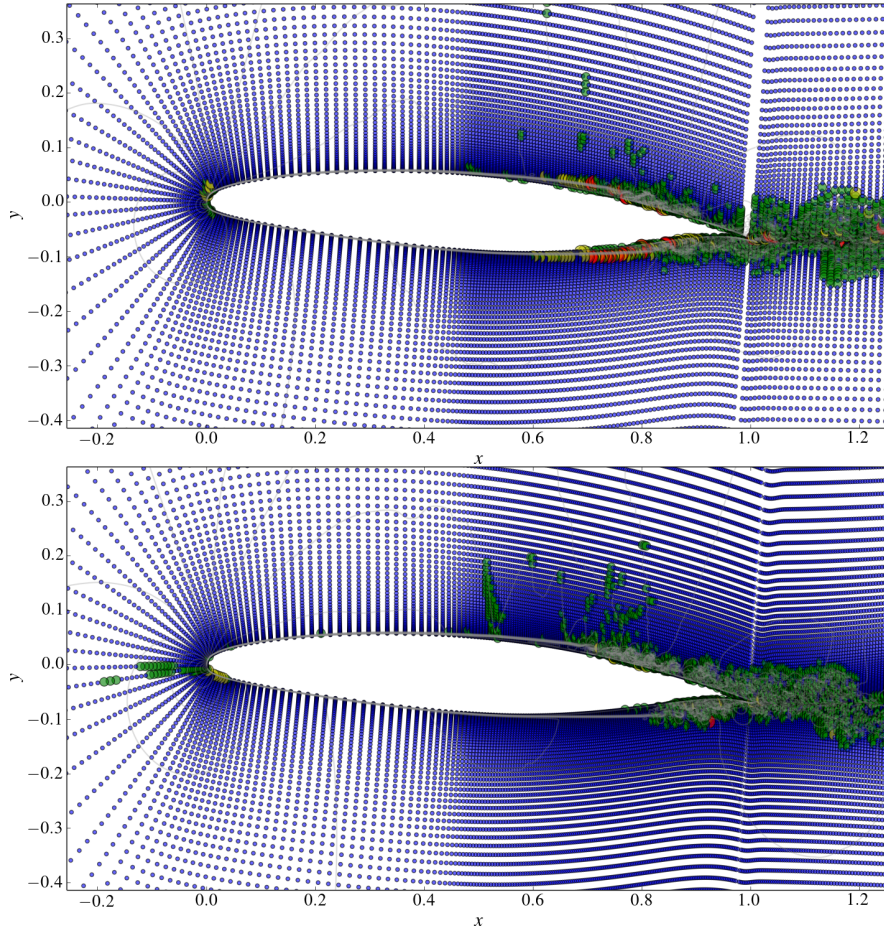


Figure 3: Contours of velocity magnitude in a two-dimensional slice of the V2C aerofoil simulation, for the initial grid (top) and the refined grid (bottom). Circles filled with blue, green, yellow and red indicate I_i error severity values of 0, 1, 2 and 3, respectively. The slices are taken at different times (after 5.33×10^6 and 6.18×10^6 timesteps, respectively).

198 5. Conclusion

199 A new error indicator has been developed for the purpose of determining
 200 where grid refinement needs to take place in order to ensure solution accuracy
 201 and stability in finite difference solutions of partial differential equations, here
 202 the compressible Navier-Stokes equations. It was found that both versions
 203 of the indicator (integer-based and floating point-based) correctly demon-
 204 strated a reduction in error severity when the grid was refined uniformly in

205 a three-dimensional Taylor-Green vortex test case. Its application to a V2C
 206 industrial use case further demonstrated its usefulness by suggesting that
 207 grid refinement was particularly necessary at the trailing edge of the aerofoil
 208 where turbulent eddy shedding occurs and along the wake path. The indi-
 209 cator developed in this paper could potentially be used in conjunction with
 210 adaptive grid refinement techniques to dynamically alter the resolution as a
 211 simulation progresses, thereby enhancing the efficiency of the model.

212 6. Acknowledgments

213 CTJ and SPJ were supported by a European Commission Horizon 2020
 214 project grant entitled “ExaFLOW: Enabling Exascale Fluid Dynamics Sim-
 215 ulations” (671571). DJL was supported by an EPSRC Centre for Doctoral
 216 Training grant (EP/L015382/1). NDT was supported by an EPSRC grant
 217 entitled “Unsteady aerodynamics of wings in extreme conditions” (EP/M022692/1).
 218 Computer time was provided by an ARCHER Leadership grant entitled
 219 “Transonic flow over an aerofoil” (e509). The data behind the results pre-
 220 sented in this paper will be available from the University of Southampton’s
 221 institutional repository. The authors thank the NVIDIA Corporation for
 222 donating the Tesla K40c GPU used for this research.

223 References

- 224 [1] A. E. Honein, P. Moin, Higher entropy conservation and numerical sta-
 225 bility of compressible turbulence simulations, *Journal of Computational*
 226 *Physics* 201 (2) (2004) 531–545. doi:10.1016/j.jcp.2004.06.006.
- 227 [2] C. Mavriplis, *A Posteriori Error Estimators for Adaptive Spectral Ele-*
 228 *ment Techniques*, Vieweg+Teubner Verlag, Wiesbaden, 1990, pp. 333–
 229 342. doi:10.1007/978-3-663-13975-1_34.
- 230 [3] S. Pirozzoli, Numerical Methods for High-Speed Flows, *Annual Review*
 231 *of Fluid Mechanics* 43 (1) (2011) 163–194.
- 232 [4] C. T. Jacobs, S. P. Jammy, N. D. Sandham, OpenSBLI: A framework
 233 for the automated derivation and parallel execution of finite difference
 234 solvers on a range of computer architectures, *Journal of Computational*
 235 *Science* 18 (2017) 12–23. doi:10.1016/j.jocs.2016.11.001.

- 236 [5] J. DeBonis, Solutions of the Taylor-Green Vortex Problem Using High-
237 Resolution Explicit Finite Difference Methods, in: 51st AIAA Aerospace
238 Sciences Meeting including the New Horizons Forum and Aerospace Ex-
239 position, Aerospace Sciences Meetings, 2013. doi:10.2514/6.2013-382.
- 240 [6] J. Sznajder, T. Kwiatkowski, Analysis of effects of shape and location
241 of micro-turbulators on unsteady shockwave-boundary layer interaction
242 in transonic flow, in: Proceedings of the VII European Congress on
243 Computational Methods in Applied Sciences and Engineering, 2016.
- 244 [7] J. P. Boyd, The Energy Spectrum of Fronts: Time Evolution of Shocks
245 in Burgers' Equation, *J. Atmos. Sci* 49 (2) (1992) 128–139.
- 246 [8] Z. Wang, K. Fidkowski, R. Abgrall, F. Bassi, D. Caraeni, A. Cary, H. De-
247 coninck, R. Hartmann, K. Hillewaert, H. Huynh, N. Kroll, G. May, P.-O.
248 Persson, B. van Leer, M. Visbal, High-order CFD methods: current sta-
249 tus and perspective, *International Journal for Numerical Methods in*
250 *Fluids* 72 (8) (2013) 811–845. doi:10.1002/fld.3767.
- 251 [9] L. E. Jones, Numerical studies of the flow around an airfoil at low
252 Reynolds number, Ph.D. thesis, University of Southampton (2008).
- 253 [10] R. Sandberg, N. Sandham, Nonreflecting zonal characteristic boundary
254 condition for direct numerical simulation of aerodynamic sound, *AIAA*
255 *J.* 44 (2) (2006) 402–405.
- 256 [11] H. Sandhu, N. D. Sandham, Boundary conditions for spatially growing
257 compressible shear layers, Report QMW-EP-1100, Faculty of Engineer-
258 ing, Queen Mary and Westfield College, University of London (1994).
- 259 [12] M. H. Carpenter, D. Gottlieb, S. Abarbanel, Time-Stable Boundary
260 Conditions for Finite-Difference Schemes Solving Hyperbolic Systems:
261 Methodology and Application to High-Order Compact Schemes, *Journal*
262 *of Computational Physics* 111 (2) (1994) 220–236.
- 263 [13] Y. Yao, Z. Shang, J. Castagna, N. D. Sandham, R. Johnstone, R. D.
264 Sandberg, V. Sponitsky, J. A. Redford, L. E. Jones, N. De Tullio, Re-
265 Engineering a DNS Code for High-Performance Computation of Tur-
266 bulent Flows, in: Proceedings of the 47th AIAA Aerospace Sciences
267 Meeting including The New Horizons Forum and Aerospace Exposition,
268 Aerospace Sciences Meetings, 2009. doi:10.2514/6.2009-566.